

An annealing algorithm to correct positioning errors in ptychography

A.M. Maiden^{a,b,*}, M.J. Humphry^b, M.C. Sarahan^c, B. Kraus^c, J.M. Rodenburg^a

^a Department of Electrical & Electronic Engineering, University of Sheffield, S1 3JD, UK

^b Phase Focus Ltd., Electric Works, Sheffield Digital Campus, Sheffield S1 2BJ, UK

^c Gatan Inc., 5794 W. Las Positas Boulevard, Pleasanton, CA 94588, USA

ARTICLE INFO

Article history:

Received 29 March 2012

Received in revised form

29 May 2012

Accepted 4 June 2012

Available online 13 June 2012

Keywords:

Coherent diffractive imaging

Phase retrieval

Ptychography

ABSTRACT

Ptychography offers the possibility of improving the resolution of atomic-scale (electron and X-ray) transmission microscopy without any of the demands of high quality lenses: its resolution is in theory only limited by the effective synthetic numerical aperture determined by the angular size of the detector. However, it has been realised experimentally that a major weakness of the approach is that the obtainable resolution is only as good as the accuracy to which the illuminating beam can be moved relative to the specimen. This can be catastrophic in the electron case because of thermal drift and hysteresis in the probe scan coils. We present here a computationally efficient extension of the 'ePIE' ptychographic reconstruction algorithm for correcting these errors retrospectively. We demonstrate its effectiveness using simulations and results from visible light and electron beam experiments that show it can correct positioning errors tens of times larger than the pixel size in the resulting image.

© 2012 Elsevier B.V. All rights reserved.

1. Introduction

Ptychography is a type of phase retrieval in which a target specimen is translated to a series of positions relative to a localised probe wavefront, and a diffraction pattern is recorded for each specimen position [1]. Provided the areas of the sample illuminated by the probe overlap substantially (preferably more than 60%), these diffraction patterns can be used in conjunction with iterative algorithms [2–5] to recover a large field of view, complex-valued image, quantitative in both modulus and phase. Ptychography, in its modern guise as a form of coherent diffractive imaging, has become popular amongst the X-ray community, see for example [6–13]. It has been put to use at visible-light wavelengths [14–17] and was first demonstrated using electrons in [18], leading to recent demonstrations of atomic-scale resolution [19,20].

Ptychographic imaging is highly robust, especially when compared to single-shot phase retrieval, but this robustness is balanced by a limitation: the resolution and accuracy of ptychographic images are restricted by the precision with which the specimen positions can be measured. For ptychography to be successful as a high-resolution imaging tool at the short wavelengths of X-ray and electron microscopy, this issue must be addressed [19–23].

A process of correcting errors in the measured specimen positions using conjugate gradient optimisation has been presented

previously [3] and a method based on Genetic Algorithms has also been trialled in simulation [24]; these approaches have not yet been shown to operate robustly using real data. A recently reported technique [22] used reference points to correct for drift in an X-ray ptychography experiment, but this required considerable complication of the usually straightforward data collection procedure. Here we detail an adaptation of the authors' previously published extended Ptychographical Iterative Engine (ePIE) [5] that, using conventionally gathered ptychographic data, robustly corrects errors in the measured specimen positions in real-world experiments, significantly improving the resolution and quality of the resulting images. Our method takes advantage of the unique serial manner in which the ePIE operates (see [5]) and typically only increases the computation time required to generate an image by 75–100% (depending on the number of iterations and the parameters used) over the ePIE itself. We demonstrate our method first using simulated ptychographic data to illustrate its operation, then using data from visible-light experiments. We also report results from experiments using a modified Scanning Electron Microscope (SEM) [20], where the algorithm was used to correct for significant non-linear drift of the sample during data collection. It is straightforward to extend the technique we present to correct for global errors such as inaccurate measurement of distances in the experiment or a rotational error between the axis of the detector and that of the specimen translation stage. We demonstrate this capability using a poorly aligned visible light experiment in which a particularly inaccurate motorised translation stage was employed.

The paper is organised as follows: Section 2 details the reconstruction algorithm, Section 3 the simulation results, Section 4 the

* Corresponding author at: Phase Focus Ltd., Electric Works, Sheffield Digital Campus, Sheffield, S1 2BJ, UK.

E-mail address: andrew.maiden@phasefocus.com (A.M. Maiden).

experimental results and Section 5 the extension to the algorithm and associated visible light results. Section 6 concludes.

2. The position-correcting algorithm

The inputs to our algorithm, which we will refer to as the position-correcting Ptychographical Iterative Engine (pcPIE), comprise a set of $j = 1 \dots J$ diffracted intensities, $I_j(\mathbf{u})$; initial estimates of both the probe and the specimen denoted as $P(\mathbf{r})$ and $O(\mathbf{r})$ respectively (we will call the ptychographic image of the specimen the 'object'); the inaccurate measured positions of the specimen during recording of each diffraction pattern, $\mathbf{R}_j = (R_{x,j}, R_{y,j})$ and a set of corrections to these measured positions, $\mathbf{C}_j = (C_{x,j}, C_{y,j})$, which are initialised to zero and are updated as the pcPIE progresses. Here $\mathbf{u} = (u, v)$ is a reciprocal space coordinate vector addressing the pixels in the plane of the diffraction pattern measurement and $\mathbf{r} = (x, y)$ a real space coordinate vector addressing pixels in the plane of the object.

The pcPIE iteratively updates the initial object and probe identically to the ePIE, but additionally and simultaneously updates the position correction vectors, attempting to correct the measured specimen positions—Fig. 1 shows a flowchart of its operation.

In the following a single iteration of the pcPIE is described; 500 such iterations were carried out to produce the results presented in Sections 3–6. Beginning with $j=1$ (we will assume here that the diffraction patterns are addressed in sequence, although in reality the order in which they are addressed should be randomised [5]) the algorithm first forms an estimate, $\psi_0(\mathbf{r})$, of the wavefront that resulted in the measured diffracted intensity $I_j(\mathbf{u})$, using the current value of the correction vector \mathbf{C}_j

$$\psi_0(\mathbf{r}) = O(\mathbf{r} - (\mathbf{R}_j + \mathbf{C}_j))P(\mathbf{r}). \quad (1)$$

Although the algorithm is described in terms of a shift of the object, shifting the probe results in an entirely equivalent wavefront; the implementation of the shifts from which the results shown here were generated (including sub-pixel shifts) was coded as in [17].

A set of $m = 1 \dots M$ further estimates of the wavefront that resulted in $I_j(\mathbf{u})$ are also computed, each with a different trial offset, of the form $c\Delta_m$, applied to \mathbf{C}_j . Here each $\Delta_m = [\delta_{x,m}, \delta_{y,m}]$ is a vector of two random numbers between ± 1 . The variable c begins at a predefined value but is decreased linearly to a small (or zero) value over a set number of iterations of the pcPIE—the effect of this variable on the algorithm's performance will be investigated in Section 3. The $m = 1 \dots M$ wavefront estimates are

then computed as

$$\psi_m(\mathbf{r}) = O(\mathbf{r} - (\mathbf{R}_j + \mathbf{C}_j + c\Delta_m))P(\mathbf{r}). \quad (2)$$

Next, $\psi_0(\mathbf{r})$ and each $\psi_m(\mathbf{r})$ is forward-propagated to give $M+1$ estimates of the wavefront incident upon the detector when $I_j(\mathbf{u})$ was recorded

$$\Psi_m(\mathbf{u}) = \mathcal{F}[\psi_m], \quad m = 0 \dots M, \quad (3)$$

where \mathcal{F} is the Fourier transform operation.

The modulus of each $\Psi_m(\mathbf{u})$ is compared to $\sqrt{I_j(\mathbf{u})}$ to give a set of errors

$$E(m) = \sum_{\mathbf{u}} |\Psi_m(\mathbf{u}) - \sqrt{I_j(\mathbf{u})}|^2. \quad (4)$$

The index of the minimum value of $E(m)$ is labelled n , so that

$$n = \arg \min_m E(m). \quad (5)$$

The modulus of the wavefront $\Psi_n(\mathbf{u})$ that resulted in the lowest error value is replaced by $\sqrt{I_j(\mathbf{u})}$ and back-propagated using the inverse Fourier transform to give an updated estimate of the exit wavefront at the plane of the object

$$\psi'(\mathbf{r}) = \mathcal{F}^{-1} \left[\sqrt{I_j(\mathbf{u})} \frac{\Psi_n(\mathbf{u})}{|\Psi_n(\mathbf{u})|} \right]. \quad (6)$$

If one of the trial offsets to \mathbf{C}_j , the current correction vector, has resulted in a lower error (i.e. $n \neq 0$), $c\Delta_n$ is used to update \mathbf{C}_j accordingly

$$\mathbf{C}_j \leftarrow \mathbf{C}_j + c\Delta_n. \quad (7)$$

Using the revised wavefront and correction vector of Eqs. (6) and (7), two update functions provide a revised object and probe

$$\begin{aligned} O(\mathbf{r} - (\mathbf{R}_j + \mathbf{C}_j)) &\leftarrow O(\mathbf{r} - (\mathbf{R}_j + \mathbf{C}_j)) + \alpha \frac{P^*(\mathbf{r})}{|P(\mathbf{r})|_{\max}^2} (\psi'(\mathbf{r}) - \psi_n(\mathbf{r})), \\ P(\mathbf{r}) &\leftarrow P(\mathbf{r}) + \beta \frac{O^*(\mathbf{r} - (\mathbf{R}_j + \mathbf{C}_j))}{|O(\mathbf{r} - (\mathbf{R}_j + \mathbf{C}_j))|_{\max}^2} (\psi'(\mathbf{r}) - \psi_n(\mathbf{r})), \end{aligned} \quad (8)$$

here α and β are constants (both fixed at a value of 1 throughout this paper) that can be used to improve convergence—further details can be found in [5].

The process above repeats for $j = 2, 3 \dots J$, until each pattern has been addressed, completing an iteration of the algorithm. Together with a revised probe and object, the result of this first iteration is a revised set of correction vectors, \mathbf{C}_j , which will be used as the centre-points of the M trial offsets in the following

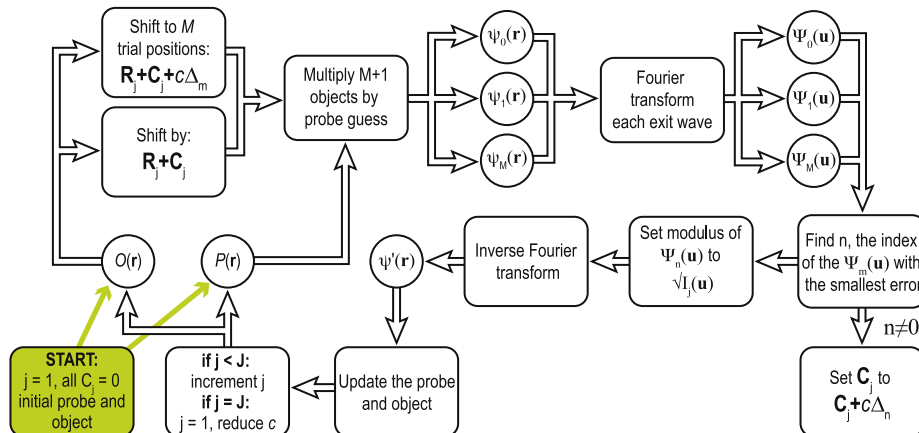


Fig. 1. A schematic representation of the position-correcting algorithm. During each loop a set of corrections to the measured specimen positions are trialed. If one of these corrections results in a better match between the measured diffraction patterns and the diffraction patterns modelled by the algorithm, it is accepted and becomes the centre-point for the trial correction offsets in the following iteration.

iteration. After each iteration the value of c is reduced by a set amount, such that it falls to a small preset value after a specified number of iterations. In this way each C_j undergoes a random walk, homing in on a value that produces the smallest difference between the reconstructed and measured diffraction pattern intensities. By reducing c the steps in this random walk slowly reduce, refining the accuracy of the correction vectors.

3. Simulation results

Before applying the pcPIE to real-world data, we first illustrate its operation and evaluate its robustness using diffraction patterns simulated from the test image shown in Fig. 2a (modulus) and 2b (phase)—the modulus and phase of the simulated probe

are shown in the respective insets to the figure. The parameters used for the simulations are arbitrary but were chosen to realistically model a visible-light experiment, with a wavelength of 500 nm, a probe approximately 300 μm in diameter, an object–detector distance of 10 cm and a 2 cm^2 detector of 512×512 pixels, giving a real-space pixel pitch of 2.5 μm . Far-field diffraction patterns were simulated at each position on a slightly distorted 20×20 grid with a nominal step size of 75 μm , as shown by the white dots in Fig. 2a. (Distortion of the grid is necessary to avoid the so-called ‘raster grid pathology’ [25] and has similarly been applied in the visible light and electron results presented below.) The region of the test image thus covered by the probe was as shown by the highlight in Fig. 2a (the white circle approximates the extent of the probe). To accommodate the possibility that the position corrections made as the pcPIE

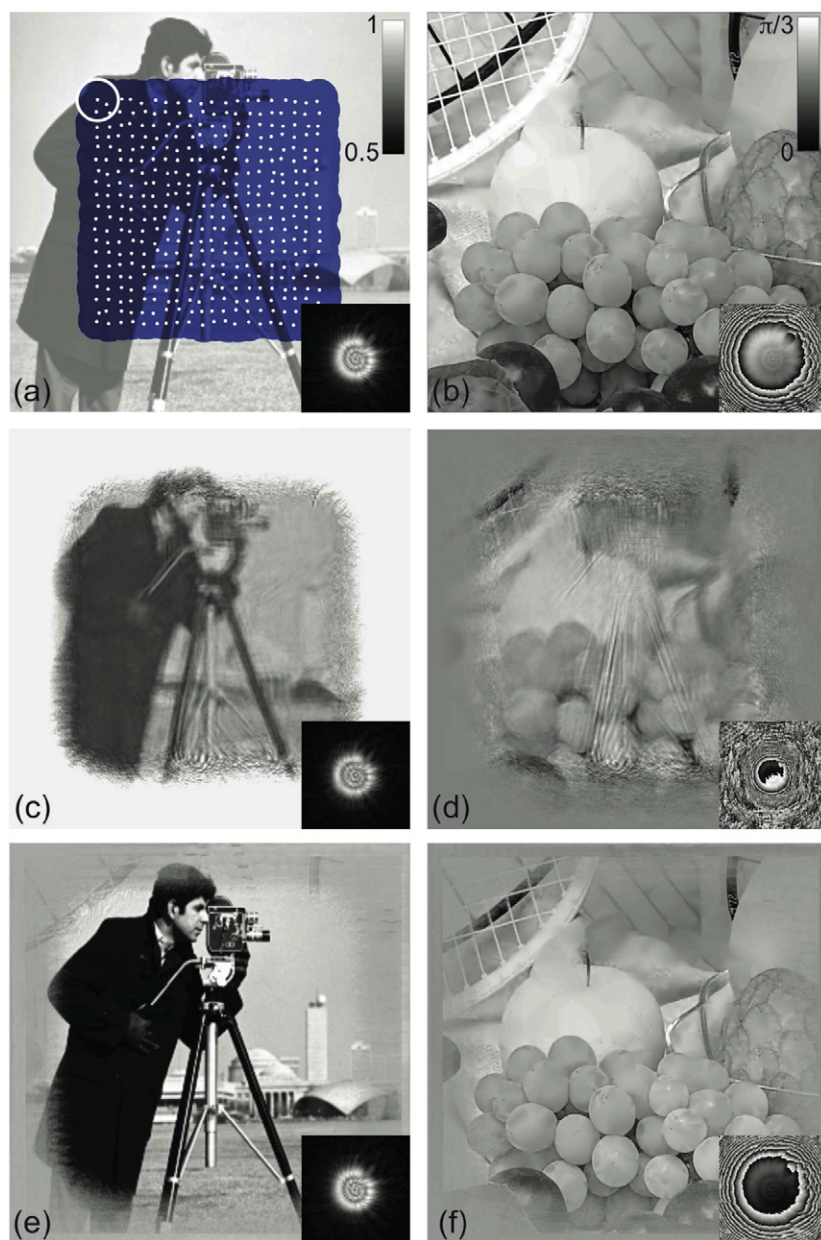


Fig. 2. Results from the pcPIE using simulated data. (a) Modulus and (b) phase of the image used to generate the simulated diffraction patterns, the insets show the modulus and phase of the simulated probe. The white dots in (a) show the grid of positions used in the simulation and the highlighting shows the overall area illuminated by the probe; the white circle shows the probe's approximate extent. (c) Modulus and (d) phase of the ePIE reconstruction after errors have been introduced into the position grid. (e) Modulus and (f) phase of the pcPIE reconstruction, after correcting these position errors.

progresses may result in a net expansion of the original position grid, the test image was made 200 rows and columns larger than that would be required by the ePIE.

After the diffraction patterns had been computed, measurement errors were artificially introduced by offsetting each position in the 20×20 grid by a vector with random x - and y -components in the range $\pm 32.5 \mu\text{m}$ (± 13 pixels), as shown by the lighter circles in Fig. 3b. The mean distance of these inaccurate positions from the actual positions (illustrated by the crosses in Fig. 3b) was fractionally under 10 pixels. These artificially introduced inaccuracies meant that after 500 iterations the ePIE produced the modulus and phase of Fig. 2c and d (the recovered probe is shown in the figure insets). This illustrates how severely positioning errors can affect ptychographic reconstructions.

The pcPIE was also allowed to run for 500 iterations. For the first 25 iterations the vectors \mathbf{C}_j were held at zero, so that no

position refinement was carried out. For the following 150 iterations the correction vectors were updated by the pcPIE using values $M=4$ and $c=25 \mu\text{m}$ (or 10 pixels). c was linearly reduced during this period to $0.125 \mu\text{m}$ (0.05 pixels) and was held at this value for the remaining 325 iterations.

The pcPIE-reconstructed image is shown in Fig. 2e (modulus) and f (phase), again with the recovered probe shown in the insets. The improvement over the ePIE reconstruction is clear and is quantified in Fig. 3. In Fig. 3a the mean distance between the known correct positions used to generate the simulated diffraction patterns and the positions as used by the ePIE and as corrected by the pcPIE are plotted as the algorithms progress (the scale for these plots is to the right of the figure). After the initial 25 iterations, when the position correction begins, the mean position error for the pcPIE falls within the next 150 iterations to less than a single pixel, falling to 0.11 pixels by the final iteration. (Of course the positions are not corrected by the ePIE, and so its position error plot remains constant.) The maximum error between the pcPIE-recovered and the actual positions was 1.24 pixels and the minimum 0.013 pixels, the standard deviation of the error was 0.17 pixels. On the same axes the diffraction pattern error is also plotted, showing how the pcPIE drives the reconstruction so as to match as closely as possible the recorded data, with the final error almost 1000 \times less than that of the ePIE. The diffraction pattern error is given by

$$E_{\text{dp}} = \frac{\sum_j \sum_{\mathbf{u}} (\sqrt{I_j(\mathbf{u})} - |\Psi_j(\mathbf{u})|)^2}{\sum_j \sum_{\mathbf{u}} I_j(\mathbf{u})}, \quad (9)$$

where each Ψ_j is calculated using the current value of the correction vector \mathbf{C}_j .

Using the same test image and probe shown in Fig. 2a and b further simulations were carried out to evaluate the pcPIE under a range of conditions, with Fig. 4 detailing the results. In each case the algorithm was run for 500 iterations, with no position updates during the first 25 iterations. The erroneous positions from Fig. 3b were used throughout (except in Fig. 4c); the dotted inset to Fig. 4a displays for purposes of comparison the mean error (~ 10 pixels) in these positions relative to the correct positions, with the error bars extending 1 standard deviation either side of this mean. A value of $M=4$ was used to generate the results in every case apart from Fig. 4d, where M itself was varied. A value of $c=25 \mu\text{m}$ was used for all but Fig. 4b (where c itself was varied) and c (where c was varied as described below) and in all cases was set to fall linearly over 150 iterations to $0.125 \mu\text{m}$.

In the simulations leading to Fig. 4a Poisson noise was introduced into the simulated diffraction patterns and the mean counts per diffraction pattern reduced in steps from 10^9 to 10^4 . The plot shows the mean error in the positions recovered by the pcPIE as the mean counts per diffraction pattern were reduced, with error bars indicating ± 1 standard deviation. It is not until the counts per diffraction pattern falls below 5×10^5 that this mean error increases above a single pixel: the diffraction patterns at this count level are substantially zero, with only a small fraction close to the centre of each pattern registering any counts at all.

In Fig. 4b the effect of the scaling constant c on the pcPIE is examined and found to be negligible. For the real experiments presented later, several values of c were tested and the one that resulted in the lowest diffraction pattern error was selected; again there was a large range of values from which similar improvements in the quality of the resulting reconstruction were achieved. If such an estimate can be made, a useful rule of thumb is to initially set c close to the mean expected positioning error.

In Fig. 4c the errors introduced into the correct positions were increased, so that the mean position error rose from 1 pixel to

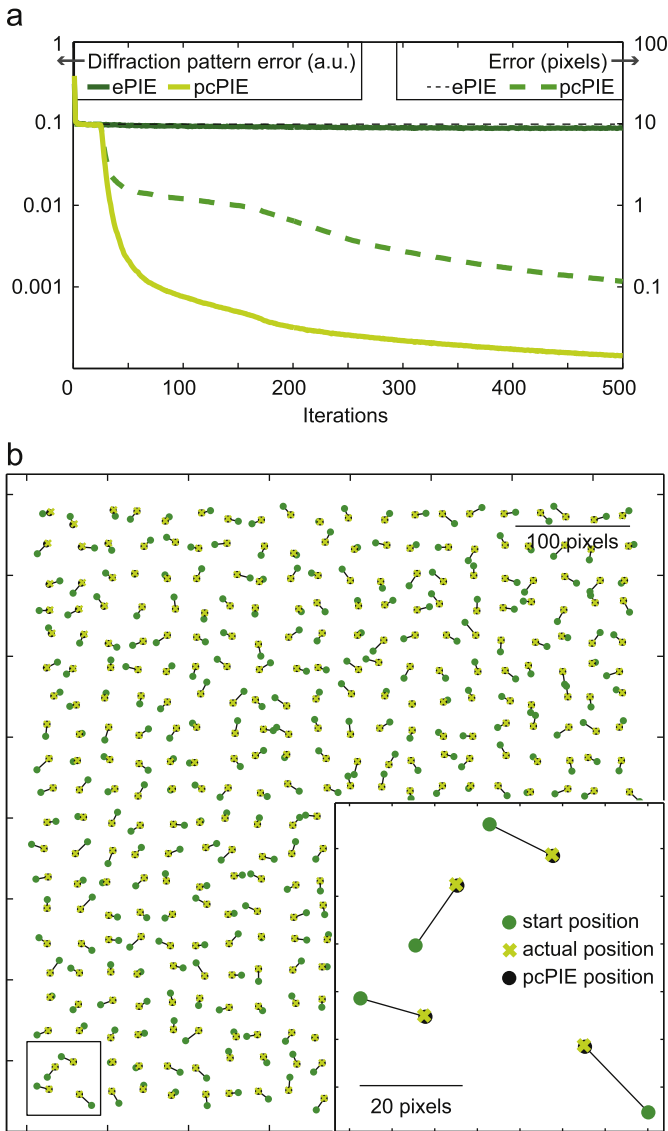


Fig. 3. Detail of the pcPIE reconstruction. (a) Graphs showing how the pcPIE corrects errors in the specimen positions and reduces the diffraction pattern error metric. The dotted traces (right-hand scale) show the mean distance in pixels of the true object positions from those used by the ePIE and pcPIE. For the ePIE, this mean distance cannot vary from its initial level of ~ 10 pixels—the pcPIE error reduces from this level to an average of ~ 0.1 pixels over the course of 500 iterations. (b) Plots of the erroneous positions provided to the two algorithms, the true object positions used in the simulation, and the pcPIE-corrected positions. The inset shows detail from the area within the box shown bottom left.

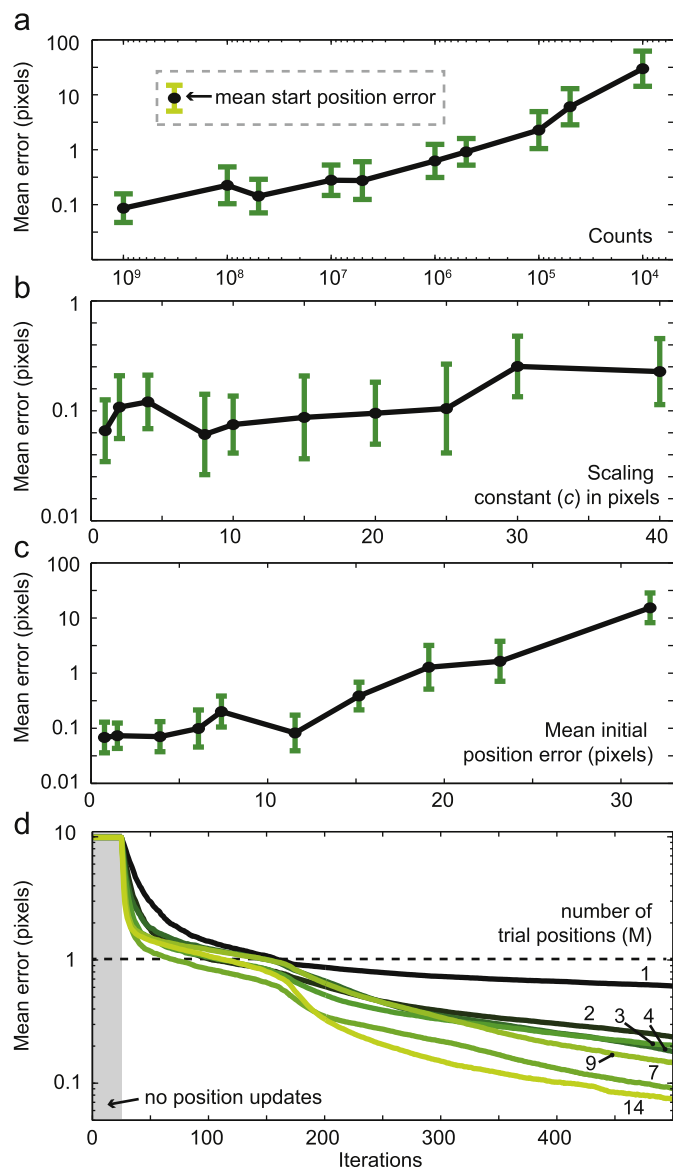


Fig. 4. An examination of the performance of the pcPIE. (a) Graph showing the performance of the pcPIE as Poisson noise is introduced into the diffraction patterns and the mean counts per diffraction pattern reduced. The inset shows the mean of the initial erroneous positions for comparison and also applies to parts (b) and (d). (b) The mean error in the pcPIE-corrected positions as the scaling constant c is increased. (c) The mean error in the pcPIE-corrected positions as the errors introduced into the correct object positions are increased. (d) The effect of the number of trial positions, M , used by the pcPIE. The error bars in each part of the figure extend to ± 1 standard deviation.

> 32. These values can be related to the nominal step size in the grid of positions, which was 30 pixels, and the approximate diameter of the probe—120 pixels. The value of c was increased accordingly for these reconstructions, being set at 3/4 of the maximum error introduced into the positions. It is only when the mean position error increases above 20 pixels, or 2/3 the grid step size, that the performance of the algorithm deteriorates notably.

In Fig. 4d the mean position error of the pcPIE is plotted over 500 iterations for a range of values of M . It is notable that the algorithm performs extremely well even for low values of M , although it converges more slowly. As a compromise between robustness and reconstruction time, a value $M=4$ generally performs well, and has been used for all of the results presented in subsequent sections. The computational overhead relative to an ePIE reconstruction depends somewhat on the size of the diffraction patterns, but in this case the

ePIE reconstruction of Fig. 2c and d took 966 s, whilst the pcPIE reconstructions for $M=1, 2, 3$ and 4 took 1129, 1431, 1733 and 2005 s respectively.

Before moving on to real-world experiments, we note an important point: for all of the simulated results, the top left corner of the reconstruction resulted in the largest remaining position errors after correction by the pcPIE. This region corresponds to an area of minimal features, so that the trial positions produce almost identical diffraction pattern errors as the algorithm progresses. Generally, in areas of free-space or areas where the specimen is not feature-rich the pcPIE is more sensitive to noise and less reliable. To bypass this issue a simple check of the variance of the object in the currently illuminated region could be made as the algorithm runs. A threshold could then be set below which there is deemed too little structure in that region to obtain reliable values from the error metric of Eq. (4), in which case modification of the corresponding position vector would be prevented.

4. Results from the optical bench and the electron microscope

An experiment was carried out on the optical bench to evaluate the pcPIE using real data. The experimental geometry was identical to that presented in [17] and employed a 675 nm laser source, a specimen-to-detector distance (camera length) of 7 cm, and a 1.5 cm^2 CCD detector, giving a pixel pitch in the reconstructed images of $3.14 \text{ }\mu\text{m}$. Although the translation stage used in this experiment was in fact highly accurate (resolution: $0.1 \text{ }\mu\text{m}$, bidirectional repeatability: $0.3 \text{ }\mu\text{m}$), positioning errors were introduced by leaving the specimen free to move on the stage, leading to positional errors caused by the abrupt stage movements. Data was collected from a randomly adjusted grid of 20×20 positions, similar to the simulated experiment detailed above. The probe in this case was $\sim 600 \text{ }\mu\text{m}$ in diameter and a nominal step size of $120 \text{ }\mu\text{m}$ was used. Our specimen was a Winter Jasmine flower bud cross-section mounted on a microscope slide.

Using this data and the programmed stage positions the ePIE produced the complex-valued image shown in Fig. 5a after 500 iterations, with the inset displaying a zoom of the area within the black box. The figure is displayed using a colourwheel, where changes in hue represent changes in phase and changes in brightness represent modulus variations; the same colourwheel scale will be used throughout to visualise the experimental results. Clearly the specimen's inertia and its insecure mounting, combined with the abrupt movements of the translation stage, have caused it to move during data collection and resulted in a blurred and distorted image.

The pcPIE was also run for 500 iterations with no position updates during the first 50 iterations and the position update parameters set to $M=4$ and $c=31 \text{ }\mu\text{m}$ (10 pixels) thereafter, with c dropping to 0 after 425 iterations. This gave the clearly improved reconstructed image of Fig. 5b, with the inset showing that fine detail down to the pixel level has been recovered by the pcPIE. The mean, minimum and maximum position corrections recovered by the pcPIE were $12.5 \text{ }\mu\text{m}$, $0.34 \text{ }\mu\text{m}$ and $109 \text{ }\mu\text{m}$ (4.0, 0.1 and 34.6 pixels) respectively.

A second experiment used the SEM detailed in [20] (a modified 30 keV FEI Quanta 600), which was equipped with a downstream camera and operated in transmission mode so that Ptychographic data could be collected by scanning the incident electron beam using the SEM scan coils. The probe was formed using the SEM condenser and objective, and under-focused by $3 \text{ }\mu\text{m}$. The probe was astigmatic, but had an average diameter of $\sim 18 \text{ nm}$; it was stepped (again with deliberately introduced small random deviations) through a grid of 51×51 positions with a 5 nm spacing. Diffraction patterns were recorded in a single exposure with a mean number of counts per pixel of approximately 400, although these counts were mostly concentrated in the central brightfield

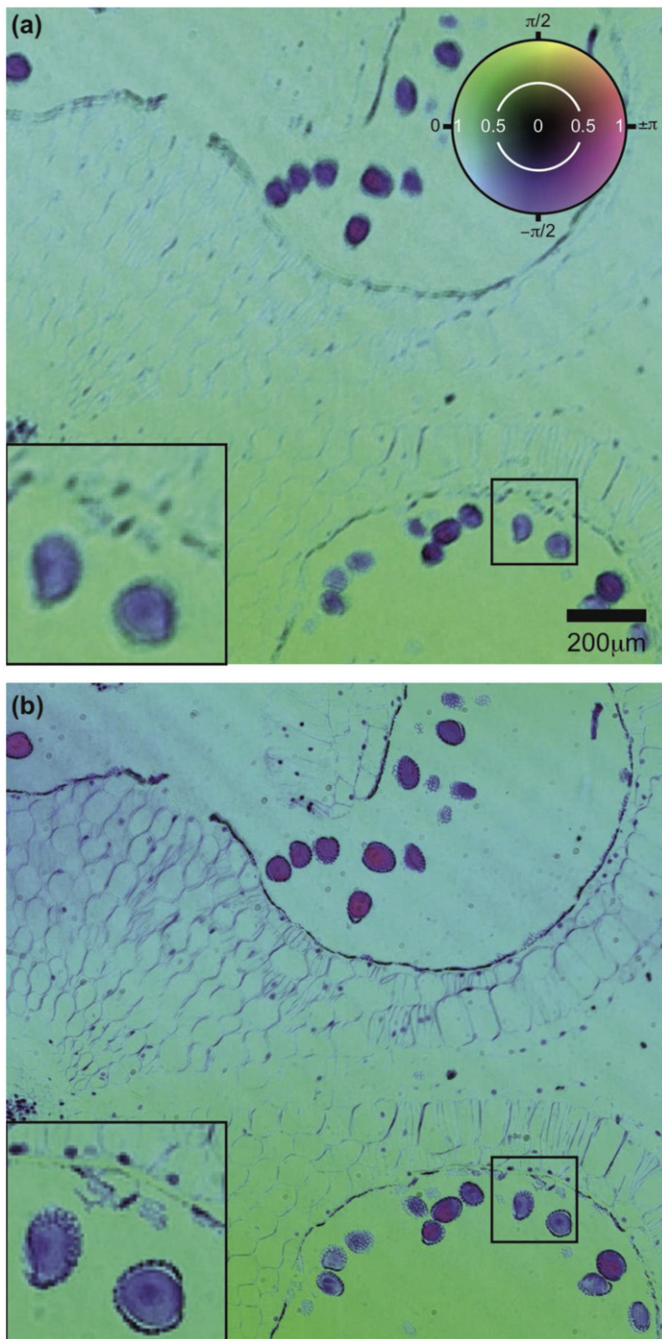


Fig. 5. Reconstructed complex-valued image of a Winter Jasmine flower bud using data collected from the optical bench with the specimen insecurely fastened to the translation stage. (a) ePIE reconstruction, (b) pcPIE reconstruction, both after 500 iterations. The insets show the areas in the black boxes bottom right of the respective figures. In the colour figure appearing in the web version of this article, the colourwheel scale shows how phase is represented by hue and modulus by brightness; the same scale is used throughout for the colour reconstructions.

disc, which had a mean number of counts per pixel of approximately 5000. The reconstructions presented here were generated using a subset of 1791 of the 2601 recorded diffraction patterns. In this experiment the specimen, a combination of gold nanoparticles and graphite clusters on a holey carbon film, moved significantly during data acquisition, presumably because of thermal drift. This meant that the ePIE produced the heavily distorted image shown in Fig. 6a—the drift is especially apparent in two strips near the middle of the reconstruction.

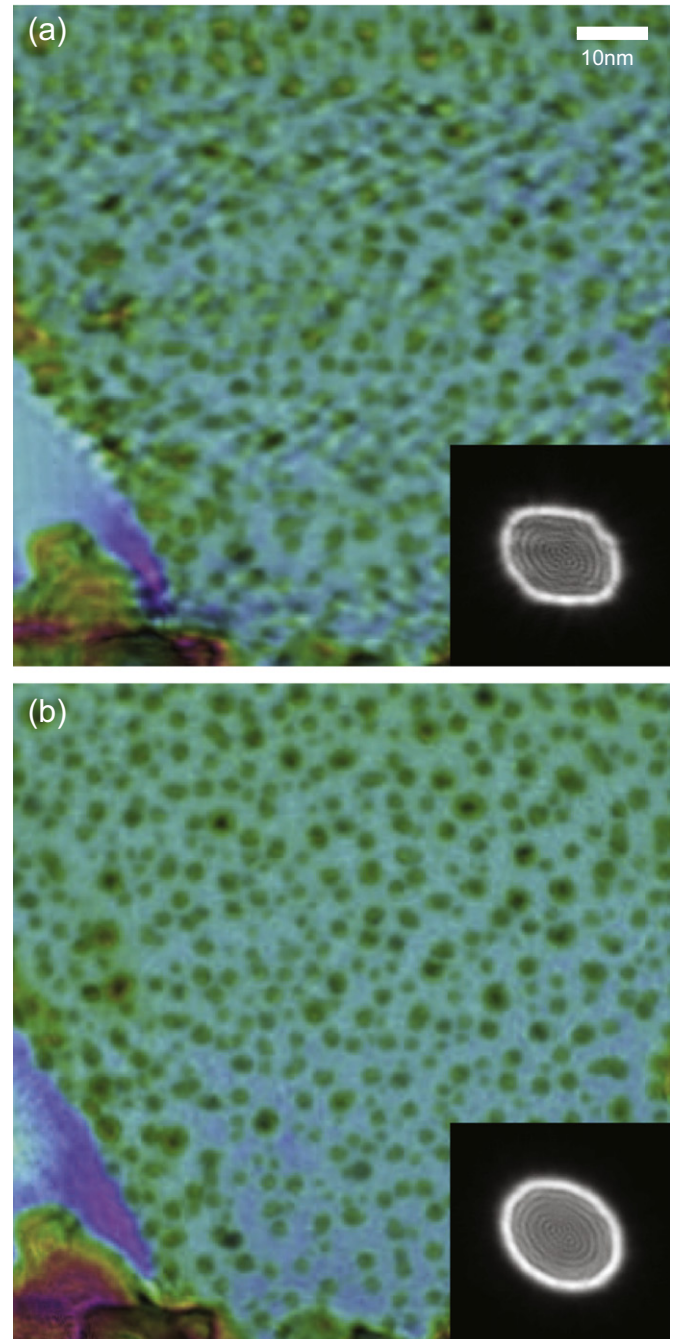


Fig. 6. Reconstructed image of a combined gold/graphite test specimen using data collected from a modified scanning electron microscope, where the specimen drifted significantly during data collection. (a) The ePIE reconstruction. (b) The pcPIE reconstruction. The insets show (on the same scale) the modulus of the probe recovered by each algorithm.

The pcPIE was run using the parameters exactly as that for the optical bench experiment, except for a change in the value of c to 1 nm (equating to 5 pixels). This produced the hugely improved reconstruction shown in Fig. 6b. In this case the mean, minimum and maximum position corrections found by the pcPIE were 2.3 nm, 0.23 nm and 6.0 nm (11.9, 1.2 and 31.4 pixels). The moduli of the probe recovered by the ePIE and by the pcPIE are shown in the insets to the respective figures and also show a significant improvement using the pcPIE.

Fig. 7 shows how the diffraction pattern error of Eq. (9) evolves over the 500 iterations of both the ePIE and the pcPIE that

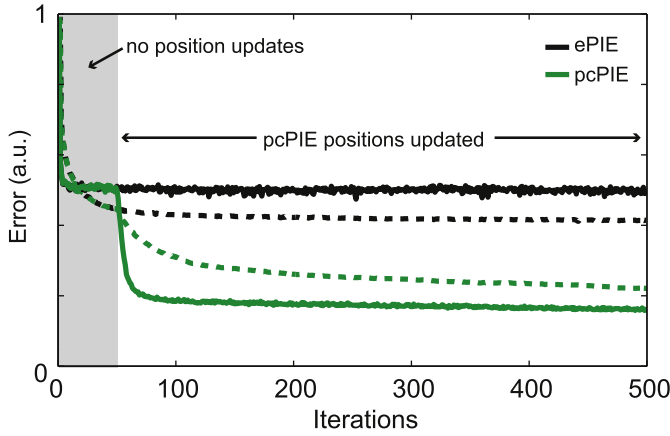


Fig. 7. Graph showing the ePIE and pcPIE diffraction pattern errors as the reconstructions of (dotted traces) Fig. 5 and (solid traces) Fig. 6 progress.

resulted in Figs. 5 and 6. In both cases the ePIE diffraction pattern error converges quickly but to a relatively high value. The pcPIE reduces this error by 50% for the Winter Jasmine reconstruction and by almost 70% for the electron beam reconstruction. Notice that for the electron reconstruction the diffraction pattern error reduced almost to its final value within 50 iterations.

5. An extension to the algorithm and a further result from the optical bench

A further addition to the pcPIE extends its operation to the correction of global positioning errors caused, for example, by a relative rotation of the positioning stage and the detector, an inaccurate measurement of the specimen–detector distance, which causes a scaling error, or a linear drift during data acquisition. We will refer to this modified algorithm as the extended pcPIE (e-pcPIE).

The e-pcPIE accounts for global position errors by decomposing each \mathbf{C}_j into a number of parts. For global rotation and scaling errors, the correction vector \mathbf{C}_{lj} and correction scalars C_r and C_s are introduced. \mathbf{C}_{lj} is identical to \mathbf{C}_j in the conventional pcPIE, with the label 'l' used to denote it as the local correction vector. C_r (in rad) and C_s are rotation and scaling correction factors respectively. C_r , C_s and every \mathbf{C}_{lj} are initialised to zero. When the e-pcPIE terminates, the corrections made to the grid of specimen positions will be a rotation by C_r radians, a scaling by $1+C_s$ and a translation by \mathbf{C}_{lj} of the j th specimen position.

As with the pcPIE, M trial offsets to the j th correction vector are generated during each pass through the loop of Fig. 2. These offsets, labelled $\mathbf{C}_{j,m}^{\text{tot}}$, are calculated according to

$$\begin{aligned} \mathbf{C}_{j,m}^{\text{tot}} = & \mathbf{C}_{lj} + c_l \mathbf{A}_{l,m} \\ & + \mathbf{R}_j \begin{bmatrix} \cos(C_r + C_r \delta_{r,m}) - 1 \\ \sin(C_r + C_r \delta_{r,m}) - 1 \end{bmatrix} \\ & + \mathbf{R}_j (C_s + C_s \delta_{s,m}), \end{aligned} \quad (10)$$

where c_l is the local random offset constant, identical to c in the base algorithm, c_r is a rotation constant (in rad) and c_s is a scale constant. Likewise, $\mathbf{A}_{l,m}$ is a vector of two random numbers in the range ± 1 identical to \mathbf{A}_m in the pcPIE, whilst $\delta_{r,m}$ and $\delta_{s,m}$ are both single random numbers chosen from the range ± 1 . c_l , c_r and c_s all reduce linearly over a preset number of iterations (which may be different for each constant) to a small or zero value. In Eq. (10) the vectors \mathbf{R}_j are assumed to have mean x and y components equal to zero—if the position grid is centred around some other value then the rotation and scaling also result in large global

translations that increase the required size of the matrix representing the object unnecessarily.

The M wavefronts of Eq. (2) are now calculated as

$$\psi_m(\mathbf{r}) = O(\mathbf{r} - (\mathbf{R}_j + \mathbf{C}_{j,m}^{\text{tot}}))P(\mathbf{r}). \quad (11)$$

The e-pcPIE then proceeds as for the pcPIE, comparing the $M+1$ candidate wavefronts against the measured diffraction intensity and selecting n , the index of the wavefront with the closest match. The correction vectors are then updated as follows:

$$\mathbf{C}_{lj} \leftarrow \mathbf{C}_{lj} + c_l \mathbf{A}_{l,n},$$

$$C_r \leftarrow C_r + c_r \delta_{r,n},$$

$$C_s \leftarrow C_s + c_s \delta_{s,n}. \quad (12)$$

Each pass through the loop of Fig. 2 therefore involves a local update to \mathbf{C}_{lj} and global updates to C_r and C_s .

It is straightforward to include further global parameters in the framework of the e-pcPIE, for example drift can be accommodated by the addition of a fourth parameter $\mathbf{C}_d = (C_{d,x}, C_{d,y})$, a drift correction vector. The following term can be then added to Eq. (10)

$$\left(j - \frac{J}{2}\right) (\mathbf{C}_d + c_d \mathbf{A}_{d,m}), \quad (13)$$

where the term $J/2$ is used to ensure the drift correction is carried out around the centre of the position grid and so does not result in a large global translation.

The remaining steps of the e-pcPIE are identical to the pcPIE: the modulus of the n th wavefront is replaced by the square-root of the j th recorded diffraction pattern and the resulting corrected wavefront is inverse Fourier transformed. The object and probe updates are implemented as in Eq. (8), with $\mathbf{C}_{j,n}^{\text{tot}}$ replacing \mathbf{C}_j .

To demonstrate the e-pcPIE diffraction data was collected from a similar optical bench setup to that used to gather the data for Fig. 5. A 633 nm laser source was used and the probe formed by imaging a 150 μm pinhole at the specimen plane. In this case however, the specimen, a lily anther mounted on a standard microscope slide, was attached to a stage known to suffer from considerable backlash and only a cursory alignment of the experiment was performed. A CCD detector ~ 16 mm downstream of the specimen recorded 512×512 pixel diffraction patterns giving a real-space pixel spacing of 1.4 μm . A grid of 10×10 specimen positions was used, with the stage instructed to follow a snake-like pattern of 45 μm steps (i.e. the first row of positions was scanned from left to right, the second from right to left and so on).

About 500 iterations of the ePIE, pcPIE and e-pcPIE were carried out. Over the first 50 iterations of the position correction algorithms, no refinement of the specimen positions was implemented. After these initial iterations had provided coarse representations of the specimen and probe, $M=4$ candidate offsets to each specimen position were generated. The constants c and c_l were set to 6.85 μm (5 pixels) and reduced to zero over the following 450 iterations. The e-pcPIE constants for the global rotation and scale factors were set to $c_r = 5^\circ$ and $c_s = 0.05$ and both reduced to zero over 200 iterations. This strategy allowed the algorithm to settle upon the correct rotation and scale factors over the first 250 iterations, and polish the finer details of the positions using the local translational offsets over the subsequent 250.

Fig. 8a shows the ePIE reconstruction resulting from this experiment; the same colourwheel scale shown in Fig. 5 is used for both the object and probe images. Although some structure is evident in the image, any fine detail has been completely corrupted. By comparison, even with the very large positional errors present the reconstructed probe wavefront shown in the inset to Fig. 8a is reasonable, although its fine fringe structure is

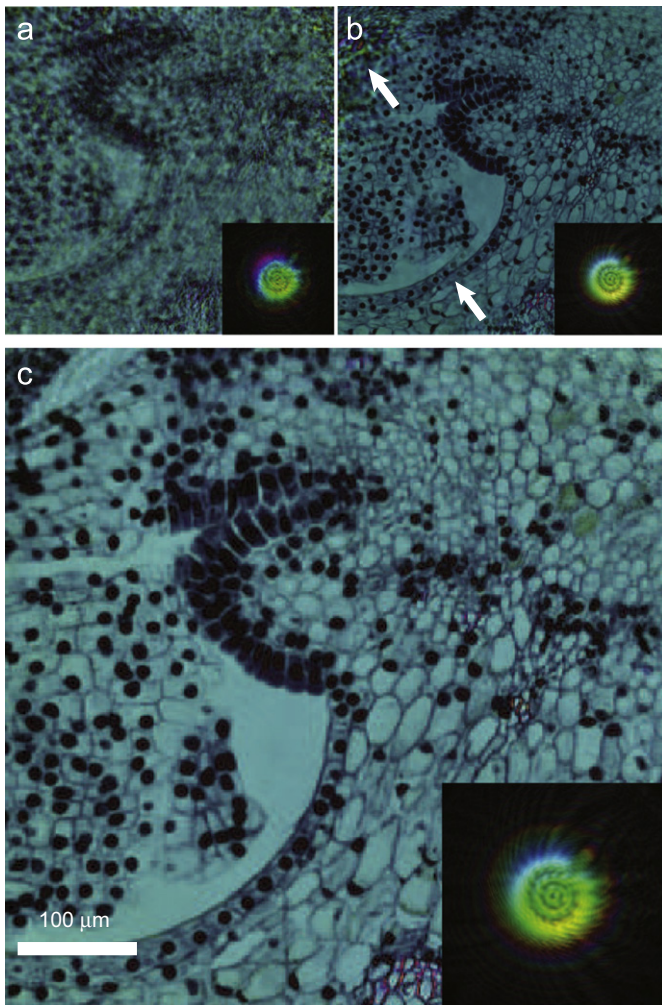


Fig. 8. Reconstructed images of a lily anther using (a) ePIE, (b) pcPIE and (c) e-pcPIE. Substantial global errors were present during this experiment; the white arrows in (b) indicate areas where they have caused problems for the pcPIE.

distorted. The improvement realised by the pcPIE is evident in Fig. 8b, and in the figure's inset where fine rings are visible in the probe phase. However the white arrows indicate two areas where the positions have not been appropriately corrected, leading to artefacts in the image: the top left corner remains distorted and the wall of the anther fractures artificially at the point indicated by the lower arrow. Locally the pcPIE has performed well, but it has been unable to tie together separate regions of the image because of the scaling and rotation errors present during this experiment.

None of the artefacts noted in Fig. 8b are present in Fig. 8c, which shows the image and reconstructed probe resulting from the e-pcPIE—Fig. 9 quantifies and provides some explanation for this improved performance.

In Fig. 9a the diffraction pattern error of Eq. (9) is plotted over the 500 iterations of the ePIE, pcPIE and e-pcPIE. The pcPIE succeeds in reducing the error level of the ePIE, but only by around 20–25% because only local position errors have been corrected. To see this, further examination of Fig. 8b reveals that the bottom left corner of the image taken alone appears accurate, but that this whole region requires a translation, scale and rotation so that it merges seamlessly with the rest of the image at the location of the lower white arrow.

The error plot for the e-pcPIE shows an initial spike when the position correction begins, followed by large fluctuations until after

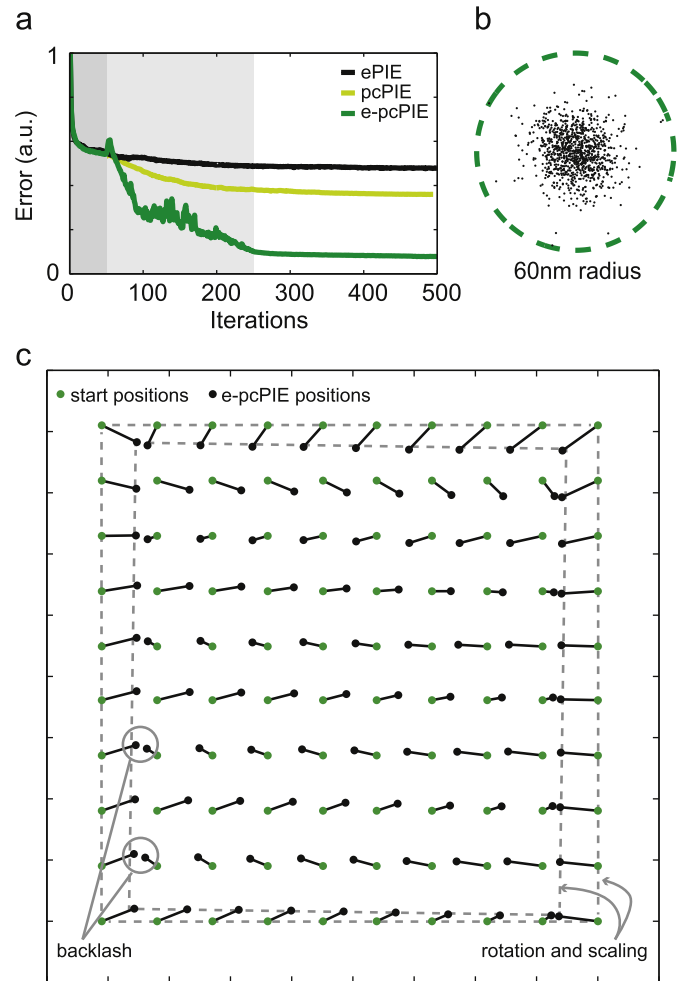


Fig. 9. Detail of the performance of the e-pcPIE for the lily anther reconstructions. (a) The diffraction pattern error of the e-pcPIE vs the ePIE and pcPIE as the algorithms progress. The shading indicates three parametric sets, from left to right: no position updates; local and global position updates; local position updates only. (b) Ten independent runs of the e-pcPIE were carried out, resulting in 10 correction vectors for each of the 100 measured specimen positions—the plot compares these sets of ten corrections to their means and shows that the e-pcPIE recovered the same positions to within 60 nm (0.04 pixels) for each of the 10 runs. (c) A graph of the corrections made to the measured specimen positions, showing how the e-pcPIE corrects significant rotation, scaling and backlash errors.

250 iterations the values of c_r and c_s reach zero. These features are a consequence of the acceptance by the algorithm of C_r and C_s values that, whilst reducing the error in Eq. (4), increase the value of the overall error given by Eq. (9). The fact that the overall error can increase and fluctuate in this way benefits the convergence properties of the e-pcPIE by allowing it to escape local minima and correct the global errors that the pcPIE misses.

To generate Fig. 9b 10 independent runs of the e-pcPIE (this time using 1000 iterations) were carried out. This resulted in a total of 1000 correction vectors—10 vectors, one per run, for each of the 100 specimen positions. The mean of each set of 10 was calculated and the offsets relative to their appropriate mean of the 1000 correction vectors are plotted in the figure. This shows that the correction vectors resulting from the 10 independent runs of the e-pcPIE were identical to within 60 nm—a remarkable degree of accuracy corresponding to 0.044 pixels. Fig. 9c shows the initial positions (lighter dots), the correction vectors (lines) and corrected positions (darker dots) from one of the 10 runs used to generate Fig. 9b. The mean, minimum and maximum corrections made to the initial positions were 21.3 μm , 8.3 μm and

35.5 μm respectively, or 15.6, 6 and 26.0 pixels. As the figure highlights, a huge amount of backlash has been corrected by the e-pcPIE, as it has a rotation error of 0.5° and a scaling of 86.5% in the x-direction and 94% in the y-direction.

6. Conclusion

We have detailed here an algorithm, the pcPIE, able to correct the positioning errors that arise during the collection of ptychographic data, which to-date have seriously limited the resolution and quality of the resulting images. We have verified the performance of our method using simulated data and demonstrated its practical application using data gathered in visible-light experiments and electron experiments using a modified SEM. An extension to the base algorithm, the e-pcPIE, has also been presented that corrects for global errors such as rotation and scaling. In a visible-light experiment this extended algorithm has been shown to be repeatable to a remarkable degree.

The decision as to whether the pcPIE or e-pcPIE should be used is based largely upon knowledge of the kind of errors that are likely to arise in a given experiment. For example, in the electron results presented in Section 4 a global drift term had already been calculated and removed from the positions using before and after reference images, and so it was not necessary to use the e-pcPIE and the drift correction term of Eq. (13). In contrast, ptychographic experiments employing a transmission electron microscope (TEM) are likely to suffer from both rotation and scaling errors caused by inaccurate calibration of the microscope camera length (changes to which causes a rotation of the diffraction patterns), whilst ptychographic scans in the X-ray regime can take several hours, making the e-pcPIE a good choice to correct for linear drift.

The primary application of the pcPIE will be at short wavelengths, especially in electron transmission microscopy, where the accurate lateral control of an electron beam is extremely difficult, and in X-ray microscopy, where the required accuracy of the specimen stages becomes increasingly difficult to realise as resolution reaches the sub-10 nm scale. Our method offers a route to maximising the ultimate resolution gains promised by ptychography.

Acknowledgements

This work was funded in part by the EPSRC Basic Technology Grant No. EP/E034055/1; 'ULTIMATE MICROSCOPY: Wavelength-Limited Resolution Without High Quality Lenses'. The authors would like to thank Phase Focus Ltd. and Gatan Inc. for technical assistance and for the use of their equipment.

References

- [1] J.M. Rodenburg, Ptychography and related diffractive imaging methods, in: Hawkes (Ed.), *Advances in Imaging and Electron Physics*, vol. 150, Elsevier, 2008, pp. 87–184.
- [2] J.M. Rodenburg, H.M.L. Faulkner, A phase retrieval algorithm for shifting illumination, *Applied Physics Letters* 85 (20) (2004) 4795–4797.
- [3] M. Guizar-Sicairos, J.R. Fienup, Phase retrieval with transverse translation diversity: a nonlinear optimization approach, *Optics Express* 16 (10) (2008) 7264–7278.
- [4] P. Thibault, M. Dierolf, A. Menzel, O. Bunk, C. David, F. Pfeiffer, High-resolution scanning X-ray diffraction microscopy, *Science* 321 (2008) 379–382.
- [5] A.M. Maiden, J.M. Rodenburg, An improved ptychographical phase retrieval algorithm for diffractive imaging, *Ultramicroscopy* 109 (10) (2009) 1256–1262.
- [6] M. Guizar-Sicairos, J.R. Fienup, Measurement of coherent x-ray focused beams by phase retrieval with transverse translation diversity, *Optics Express* 17 (4) (2009) 2670–2685.
- [7] K. Giewekemeyer, P. Thibault, S. Kalbfleisch, A. Beerlink, C. Kewish, M. Dierolf, F. Pfeiffer, T. Salditt, Quantitative biological imaging by ptychographic x-ray diffraction microscopy, *Proceedings of the National Academy of Sciences* 107 (2) (2010) 529–534.
- [8] A. Schropp, P. Boye, J.M. Feldkamp, R. Hoppe, J. Patommel, D. Samberg, S. Stephan, K. Giewekemeyer, R.N. Wilke, T. Salditt, J. Gulden, A.P. Mancuso, A. Vartanyants, E. Weckert, S. Schöder, M. Burghammer, C.G. Schroer, Hard x-ray nanobeam characterization by coherent diffraction microscopy, *Applied Physics Letters* 96 (2010) 091102.
- [9] C.M. Kewish, P. Thibault, M. Dierolf, O. Bunk, A. Menzel, J. Vila-Comamala, K. Jefimovs, F. Pfeiffer, Ptychographic characterization of the wavefield in the focus of reflective hard x-ray optics, *Ultramicroscopy* 110 (4) (2010) 325–329.
- [10] M. Dierolf, A.T.P. Menzel, P. Schneider, C.M. Kewish, R. Wepf, O. Bunk, F. Pfeiffer, Ptychographic x-ray computed tomography at the nanoscale, *Nature* 467 (2010) 436–439.
- [11] K. Giewekemeyer, M. Beckers, T. Gorniak, M. Grunze, T. Salditt, A. Rosenhahn, Ptychographic coherent x-ray diffractive imaging in the water window, *Optics Express* 19 (2) (2011) 1037–1050.
- [12] M. Beckers, T. Senkbeil, T. Gorniak, M. Reese, K. Giewekemeyer, S. Gleber, T. Salditt, A. Rosenhahn, Chemical contrast in soft x-ray ptychography, *Physical Review Letters* 107 (2011) 208101.
- [13] M. Guizar-Sicairos, A. Diaz, M. Holler, M.S. Lucas, A. Menzel, R.A. Wepf, O. Bunk, Phase tomography from x-ray coherent diffractive imaging projections, *Optics Express* 19 (2011) 21345–21357.
- [14] G.R. Brady, M. Guizar-Sicairos, J.R. Fienup, Optical wavefront measurement using phase retrieval with transverse translation diversity, *Optics Express* 17 (2) (2009) 624–639.
- [15] A.M. Maiden, J.M. Rodenburg, M.J. Humphry, Optical ptychography: a practical implementation with useful resolution, *Optics Letters* 35 (15) (2010) 2585–2587.
- [16] A.M. Maiden, M.J. Humphry, J.M. Rodenburg, A new method of high resolution, quantitative phase scanning microscopy, in: M.T. Postek, D.E. Newbury, S.F. Platek, D.C. Joy (Eds.), *SPIE Proceedings of Scanning Microscopy*, vol. 7729, 2010.
- [17] A.M. Maiden, M.J. Humphry, F. Zhang, J.M. Rodenburg, Superresolution imaging via ptychography, *Journal of the Optical Society of America A* 28 (4) (2011) 604–612.
- [18] F. Hübner, J.M. Rodenburg, A.M. Maiden, F. Sweeney, P.A. Midgley, Wave-front phase retrieval in transmission electron microscopy via ptychography, *Physical Review B* 82 (12) (2010) 121415, <http://dx.doi.org/10.1103/PhysRevB.82.121415>.
- [19] C.T. Putkunz, A.J. D'Alfonso, A.J. Morgan, M. Weyland, C. Dwyer, L. Bourgeois, J. Etheridge, A. Roberts, R.E. Scholten, K.A. Nugent, L.J. Allen, Atom-scale ptychographic electron diffractive imaging of boron nitride cones, *Physical Review Letters* 108 (2012) 073901.
- [20] M.J. Humphry, B. Kraus, A.C. Hurst, A.M. Maiden, J.M. Rodenburg, Ptychographic electron microscopy using high-angle dark-field scattering for sub-nanometre resolution imaging, *Nature Communications* 3 (2012) 730.
- [21] A. Schropp, P. Boye, A. Goldschmidt, S. Hönig, R. Hoppe, J. Patommel, C. Rakete, D. Samberg, S. Stephan, S. Schöder, M. Burghammer, C.G. Schroer, Non-destructive and quantitative imaging of a nano-structured microchip by ptychographic hard x-ray scanning microscopy, *Journal of Microscopy* 241 (1) (2010) 9–13.
- [22] Y. Takahashi, A. Suzuki, N. Zettsu, Y. Kohmura, Y. Senba, H. Ohashi, K. Yamauchi, T. Ishikawa, Towards high-resolution ptychographic x-ray diffraction microscopy, *Physical Review B* 83 (2011) 214109.
- [23] F. Hübner, J.M. Rodenburg, A.M. Maiden, P.A. Midgley, Extended ptychography in the transmission electron microscope: possibilities and limitations, *Ultramicroscopy* 111 (8) (2011) 1117–1123.
- [24] A. Shenfield, J.M. Rodenburg, Evolutionary determination of experimental parameters for ptychographical imaging, *Journal of Applied Physics* 109 (2011) 124510.
- [25] M. Dierolf, P. Thibault, A. Menzel, C.M. Kewish, K. Jefimovs, I. Schlichting, K. von Kónig, O. Bunk, F. Pfeiffer, Ptychographic coherent diffractive imaging of weakly scattering specimens, *New Journal of Physics* 12 (3) (2010) 035017.